Article

Biofunctionalized Graphene Quantum Dots Based Fluorescent Biosensor toward Efficient Detection of Small Cell Lung Cancer

Ashish Kalkal,[⊥] Rangadhar Pradhan,[⊥] Sachin Kadian, Gaurav Manik, and Gopinath Packirisamy*

Cite This: *ACS Appl. Bio Mater.* 2020, 3, 4922−4932

Read Online

ACCESS | Metrics & More | Article Recommendations | Supporting Information

ABSTRACT: Quantitative detection of cancer biomarkers with higher accuracy and sensitivity provides an effective platform for screening, monitoring, early diagnosis, and disease surveillance. The present work demonstrates the fabrication and application of fluorescent turn-on biosensor for ultrasensitive detection of small cell lung cancer biomarker utilizing biofunctionalized graphene quantum dots as the energy donor and gold nanoparticles (AuNPs) as the energy acceptor. One-pot and the bottom-up hydrothermal route have been employed for the synthesis of *in situ* amine-functionalized and nitrogen-doped graphene quantum dots (amine-N-GQDs) and further characterized experimentally by different analytical techniques. The molecular simulation studies were performed using the Material Studio software for optimizing the possible chemical structure of synthesized amine-N-GQDs, a comprehensive analysis of experimental results to validate the presence of potential N-doping and amine functionalization sites. Then monoclonal neuron-specific enolase antibodies (anti-NSE) were covalently immobilized to amine-N-GQDs to provide the biofunctionalized GQDs (anti-NSE/amine-N-GQDs). A label-free and efficient fluorescent biosensor based on nanosurface energy transfer (NSET) between anti-NSE/amine-N-GQDs and AuNPs has been developed for neuron-specific enolase (NSE) detection. The fluorescence response studies of anti-NSE/amine-N-GQDs@AuNPs nanoprobe conducted as a function of NSE antigen exhibited fast response time (16 min), broader linear detection range (0.1 pg mL^{-1} to 1000 ng mL^{-1}), and remarkably low detection limit (0.09 pg mL^{-1}). Additionally, the fluorescent biosensor exhibited excellent performance in real samples, with an average recovery value of 94.69%.

KEYWORDS: biosensor, graphene quantum dots (GQDs), energy transfer, small cell lung cancer (SCLC), biomarker
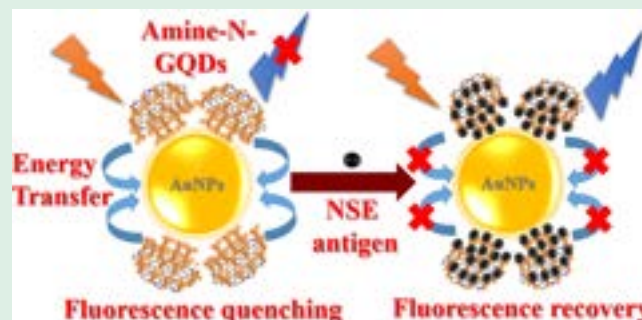
1. INTRODUCTION

Lung cancer is known to be one of the most deadly forms of cancer, causing a large number of deaths worldwide. It can be classified into two major dichotomies: small cell lung cancer (SCLC) and nonsmall cell lung cancer (NSCLC). SCLC is known for its tendency to metastasize early and rapid doubling time and is difficult to treat due to its initial high sensitivity to chemotherapy but invariable relapse and acquired chemo-resistance.[1] SCLC accounts for 15−20% of new lung cancer cases, and the majority of these cases are diagnosed at an advanced stage with serious illness.[2] Therefore, early diagnosis of SCLC is of utmost interest, providing increased chances for patient survival. In this context, the quantitative detection of elevated cancer biomarkers with higher accuracy and sensitivity provides an effective platform for screening, early diagnosis, and disease surveillance. Studies have reported that neuron-specific enolase (NSE) is a reliable, specific, and sensitive serum biomarker for the early diagnosis of SCLC and could assess the patient's recovery progress. In normal human beings, the serum NSE concentration has been recorded up to 12−13 ng mL^{-1}, whereas in SCLC patients, serum NSE concentration is found to be more than 35 ng mL^{-1}.[3] For the SCLC diagnosis, a cutoff value of 16−25 ng mL^{-1} has been reported.[1] Therefore, it is highly desirable to develop an efficient, selective, inexpensive, and sensitive diagnostic tool that can provide early and accurate NSE detection and can be used for continuous assessment.

Recently, nonradiative energy transfer (ET) based fluorescent sensors have drawn tremendous research interest in detecting the biomolecular interactions, measuring nanoscaled information in clinical applications and medical fields.[4−9] These sensors provide various advantages like rapid, reliable, and highly sensitive response with minimum background noise, easy operation, high specificity, the requirement of simple instrumentation, and capability for real-time detection.[4,10,11] It
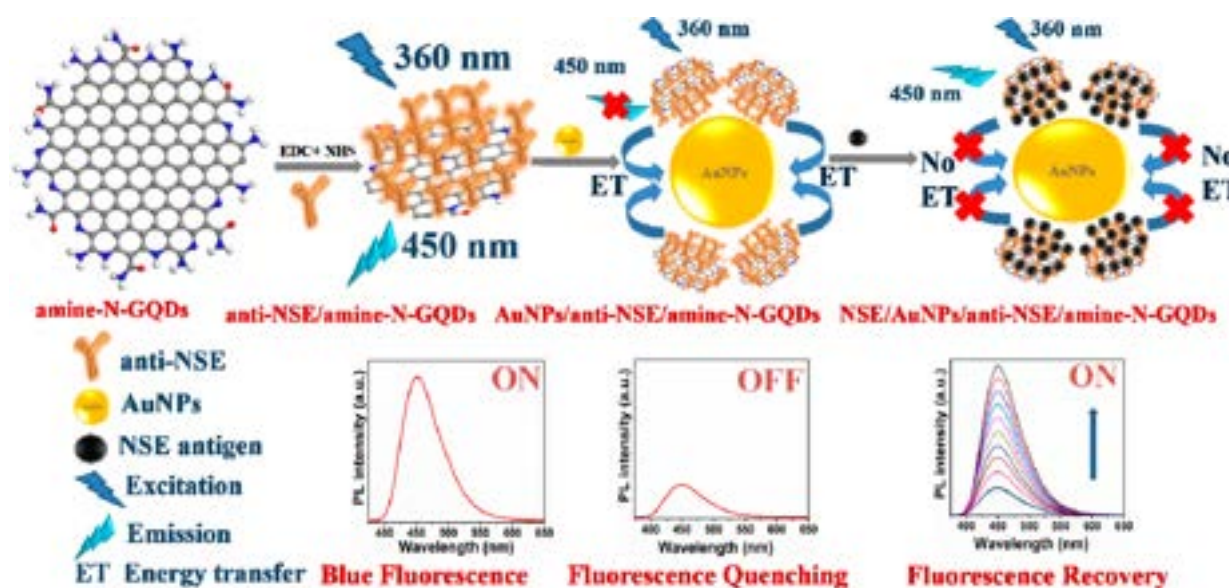
Figure 1. Pictorial representation indicating the mechanism of the fluorescent biosensor for small cell lung cancer biomarker detection.

has been reported that for enhancing the efficiency and performance of energy transfer based fluorescent biosensors, the selection of appropriate donor−acceptor pair is crucial.[12,13] In traditional Förster resonance energy transfer (FRET) based sensors, organic dyes have been widely used as energy donor−acceptor pair. However, photobleaching, small Stokes shift, narrow excitation band, long-term cytotoxic effects, and the presence of toxic precursors are the reported challenges of these materials.[14] Moreover, it has been reported that conventional FRET sensors have a limited detectable distance of ∼6 nm wherein ET efficiency follows $1/d^6$ distance (between donor−acceptor pair) dependence. Therefore, the exploration of nanomaterials based donor−acceptor pair with outstanding optical properties and excellent biocompatibility is highly demanded.[15,16] In this context, gold nanoparticles (AuNPs) have emerged as a significant energy acceptor alternative to the organic dyes, following nanosurface energy transfer (NSET) mechanism. It has been reported that in the case of NSET, the energy can be transferred over a much longer distance (up to 50 nm) following $1/d^4$ distance dependence. Recently, Chen et al. reported and reviewed that NSET is the operational energy transfer mechanism in AuNPs for the quenching of fluorescent donors.[17,18]

Similarly, carbon-based fluorescent nanomaterials, mainly graphene quantum dots (GQDs), have emerged as a promising alternative as energy donor due to their remarkable optical and electronic properties.[19−24] Compared to semiconductor quantum dots (QDs) and organic dyes, GQDs exhibit good photostability, excellent biocompatibility, excellent water solubility, tunable size-dependent PL, broad excitation spectra, strong quantum confinement, and edge effects, making them a promising material as energy donor.[19,20,25,26] However, low quantum yield (QY) and short fluorescence lifetime of GQDs restrict their practical biosensing applications.[27,28] In recent years, a heteroatom doping or surface functionalization has been reported as a powerful means to improve the electronic and optical properties of GQDs.[19] Doped GQDs have been reported with improved QY, long fluorescence lifetime, and other optical properties.[29−31]

Furthermore, the surface functionalization with primary amine molecules convert the −COOH and epoxy groups of GQDs to −CNHR and −CONHR. These groups result in suppression of nonradiative electron−hole recombination and thereby enrich intrinsic state emission.[19] Typically, compounds such as olylamine, oleic acid, 3-aminopropyltriethoxysilane (APTES), and 3-mercaptopropyltriethoxysilane (MPTES) have been widely utilized for *ex situ* surface functionalization.[32,33] However, it has been reported that *ex situ* functionalization involves an extra step in the procedure to link the required functional group that may affect the fluorescence property and morphology of QDs.[34]

Therefore, in this article, a one-pot and the bottom-up hydrothermal method has been used to obtain *in situ* amine-functionalized nitrogen-doped graphene quantum dots (amine-N-GQDs). The possible chemical structure of synthesized amine-N-GQDs has been optimized through the molecular simulation studies. Nitrogen doping and *in situ* amine functionalization have been validated using both theoretical and experimental characterization tools. Further, we have reported the biofunctionalized GQDs (anti-NSE/amine-N-GQDs) and AuNPs based fluorescent turn-on biosensor for ultrasensitive and quantitative NSE detection. The fluorescence response studies of fabricated biosensor conducted as a function of NSE antigen exhibited remarkable biosensing parameters in both standard and real samples.

2. EXPERIMENTAL SECTION

2.1. Synthesis of Amine-N-GQDs via Hydrothermal Method. Low temperature, one-pot, and the bottom-up hydrothermal method have been utilized for the synthesis of amine-N-GQDs. Briefly, 2.1 g of citric acid was dispersed in 10 mL of distilled water under magnetic stirring. Next, 3.7 mL of diethylenetriamine (DETA) was added to the above solution and continued stirring to obtain a transparent solution. The resultant solution was transferred to a Teflon-lined hydrothermal pressure vessel. Afterward, the sealed hydrothermal vessel was placed in an electric oven and heated at 170 °C for the optimized duration of 5 h. After natural cooling to room temperature, the obtained solution was filtered using a 0.2 μm syringe filter to separate the large-sized particles. Further, the obtained solution was subjected to dialysis against water for 2 days (retained MWCF: 2 kDa) to remove remaining small molecules. Finally, the resultant solution was freeze-
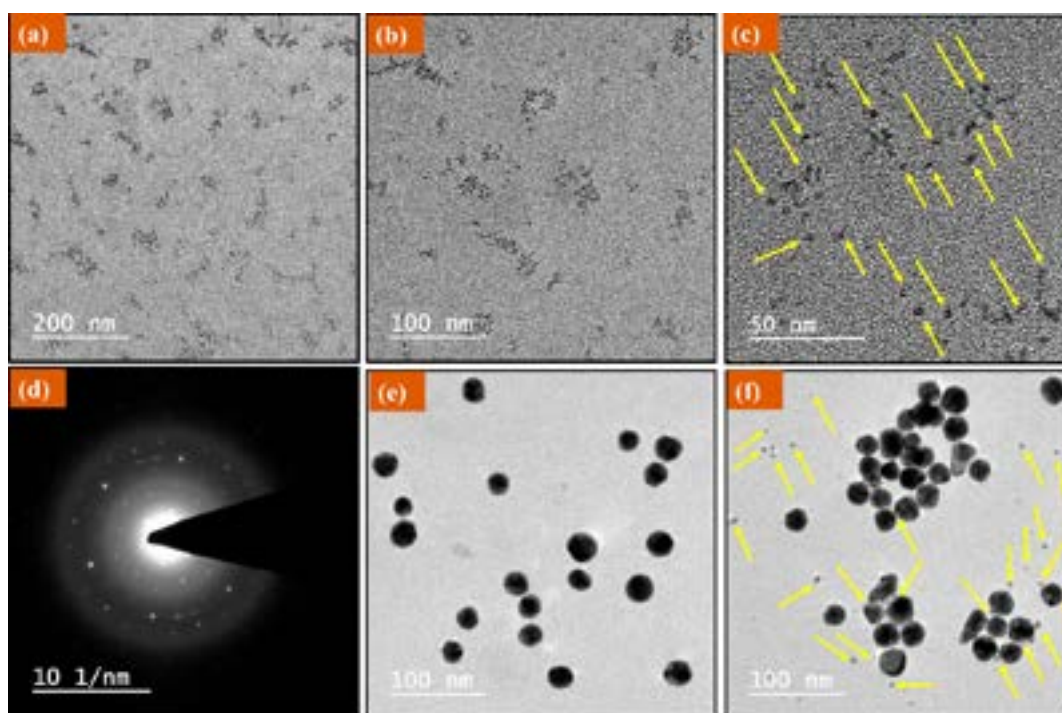
Figure 2. (a−c) TEM images of synthesized amine-N-GQDs at different scales; (d) SAED pattern of amine-N-GQDs; (e) TEM image of AuNPs; (f) TEM image of the amine-N-GQDs@AuNPs composite.

dried for 48 h to obtain the semisolid yellow amine-N-GQDs, which was further dispersed in deionized water to obtain the amine-N-GQDs stock solution and stored at 4 °C until further use. Scheme S1 illustrates the amine-N-GQDs synthesis process using the bottom-up hydrothermal method. A similar procedure was carried out for the synthesis of GQDs without adding the DETA solution.

2.2. Preparation of Anti-NSE/Amine-N-GQDs Conjugate. For this, the procedure has been adapted from Kumar et al.[35] First, monoclonal neuron-specific enolase antibodies (anti-NSE) were activated utilizing the standard EDC-NHS coupling chemistry. For this, 150 μL of anti-NSE (50 μg mL^{-1}), 75 μL of 0.2 M EDC and 0.05 M NHS were mixed and incubated at room temperature for 30 min, where NHS activated the −COOH groups present on the Fc region of the anti-NSE antibody and EDC acted as the coupling agent. The activated antibody solution was added to the diluted amine-N-GQDs (100 μg mL^{-1}) solution (1:1 v/v) and allowed to incubate at room temperature for an additional 2 h duration. The anti-NSE/amine-N-GQDs conjugate was obtained through the amide bond formation between the −COOH groups of anti-NSE and −NH$_2$ groups of amine-N-GQDs, and further characterized by UV−vis, zeta potential, and FTIR studies (details in Supporting Information, Figure S2a−c). The calculated adhesion efficiency was found to be 88.13% indicating the high ability of amine-N-GQDs for the development of efficient fluorescent biosensor (details in Supporting Information, Figure S2d).

2.3. Procedure and Mechanism of Fluorescent Biosensor for NSE Detection. The mechanism of anti-NSE/amine-N-GQDs@AuNPs based fluorescent biosensor has been schematically illustrated in Figure 1. The anti-NSE/amine-N-GQDs conjugate emits strong blue fluorescence under the exposure of 360 nm ("ON" state), which is quenched by the ultrahigh quenching efficiency of AuNPs (acceptor). In AuNPs, there are free conduction band electrons that provide dipole vectors on the surface of AuNPs, thereby accepting the donor energy.[4,36] Also, the larger surface area of AuNPs provides efficient energy transfer by using the concept of multiple-donor-single-acceptor configuration. Additionally, AuNPs do not possess definite dipole moment; therefore, energy transfer to the AuNPs can occur from the donor in any orientation. Moreover, AuNPs' broad absorption cross-sections, particularly close to their Plasmon resonance, enrich their performance as energy acceptors.[4,36,37]

An optimized amount of anti-NSE/amine-N-GQDs conjugate was mixed with AuNPs (disclosure subject to acquired patent clauses, Indian patent, Application No. 202011010110) and PL emission spectra were recorded at room temperature to observe the quenching effect ("OFF" state). Further, 50 μL of each antigen concentration was added to anti-NSE/amine-N-GQDs@AuNPs solution. The resultant solution was diluted to 1 mL with phosphate buffer saline (PBS) solution (pH 7.4) and incubated for the optimized duration of 16 min. Subsequently, PL emission spectra were measured to observe the fluorescence intensity recovery with increasing NSE antigen concentration. Upon the addition of NSE antigen, the distance between anti-NSE/amine-N-GQDs conjugate and AuNPs increases because NSE antigen binds explicitly with the anti-NSE antibody due to specific antigen−antibody interactions forming a NSE/anti-NSE/amine-N-GQDs@AuNPs immunocomplex. The formed complex obstructs the energy transfer process because the antigen−antibody interactions are stronger than the adsorption between anti-NSE/amine-N-GQDs conjugate and AuNPs, resulting in the restoration of fluorescence with the addition of increasing NSE antigen concentration ("ON" state).

3. RESULTS AND DISCUSSION

3.1. Morphological and Structural Characterizations. The obtained amine-N-GQDs have been characterized for the morphological, structural, and size distribution analysis utilizing the TEM (Figure 2a−c) and XRD analysis (Figure S1). The corresponding TEM images at different scales denote that the obtained amine-N-GQDs are nonaggregated and uniformly distributed QDs with an average size of ∼3 nm. The selected area electron diffraction (SAED) pattern (Figure 2d) shows the characteristic diffraction pattern with bright points suggesting the excellent crystallinity of synthesized amine-N-GQDs.[38] Similarly, the XRD pattern of amine-N-GQDs (Figure S1) exhibited a broad peak around 25.2°, which is consistent with 002 planes of graphene. The TEM image (Figure 2e) indicates that the AuNPs are also well distributed and round-shaped nanoparticles with an average size of ∼20
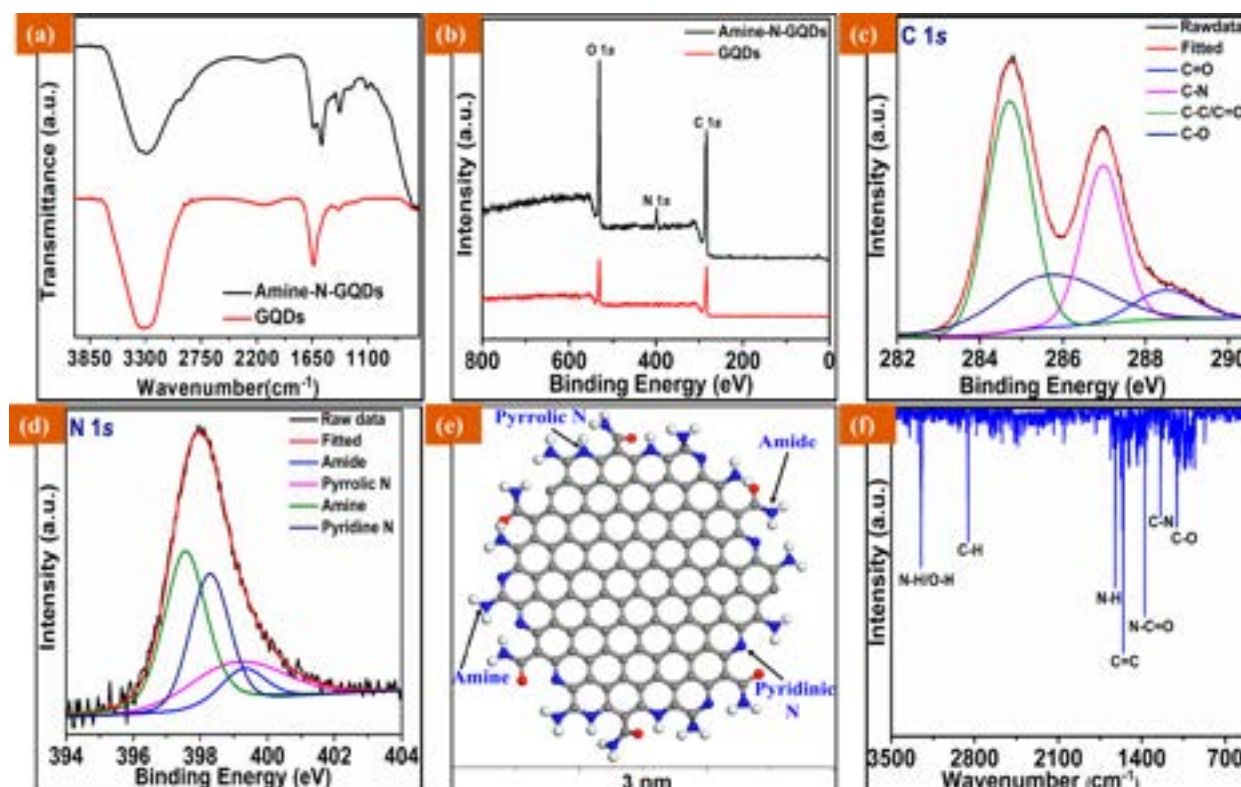
Figure 3. (a) FTIR spectra of synthesized GQDs (red line) and amine-N-GQDs (black line); (b) full scan XPS spectra of synthesized GQDs and amine-N-GQDs; (c) deconvoluted C 1s spectra of amine-N-GQDs; (d) deconvoluted N 1s spectra of amine-N-GQDs; (e) theoretically optimized structure and (f) theoretically calculated FTIR spectrum of amine-N-GQDs.

nm. Figure 2f shows the TEM image of the amine-N-GQDs@ AuNPs composite. Smaller sized amine-N-GQDs were found to surround the larger AuNPs forming a satellite structure. Further, the cytotoxicity studies of amine-N-GQDs were carried out using the MTT assay on both normal lung (L-132) and cancer (A549) cell lines (details in Supporting Information, Figure S3).

3.1.1. Fourier Transform Infrared (FTIR) and X-ray Photoelectron Spectroscopy (XPS). FTIR was performed to determine the presence of different functional groups on bare GQDs and amine-N-GQDs (Figure 3a). In both spectra, the bands obtained around 1115 cm^{-1} and 1556 cm^{-1} are assigned to C−O stretching and aromatic C=C ring stretching vibrations, respectively.[39,40] Similarly, bands obtained between 2800 and 3000 cm^{-1} are attributed to C−H stretching vibrations for both spectra. In the case of GQDs, stretching vibrations related to only O−H groups (3000−3400 cm^{-1}) were obtained, whereas in amine-N-GQDs, N−H amine/ amide stretching vibrations along with O−H vibrations were obtained.[40] In amine-N-GQDs spectra, additional peaks were acquired around 1250 and 1380 cm^{-1} due to C−N in-plane and N−C=O stretching, respectively.[39] In the case of bare GQDs, the obtained shoulder peak around 1740 cm^{-1} and intense peak around 1650 cm^{-1} indicate the presence of carboxylic groups. However, in amine-N-GQDs, the dissipation of these peaks can be attributed to the combined effect of N−H bending vibrations and amide-carbonyl (−NH−C=O) vibrations due to the formation of amide bonds through the interaction of −COOH group of GQDs as Lewis base.[40] The presence of additional amine and amide functionalities in amine-N-GQDs FTIR spectra verified its successful *in situ* amine functionalization.

Further, XPS measurements were performed to investigate the surface chemistry of GQDs and amine-N-GQDs. Figure 3b shows the full scan XPS spectra of GQDs and amine-N-GQDs. It can be observed that only carbon C 1s (∼284 eV) and oxygen O 1s (∼532 eV) peaks are present in GQDs, whereas nitrogen N 1s peaks (∼400 eV) along with carbon and oxygen peaks are present in amine-N-GQDs. Further, for the detailed analysis, the C 1s high-resolution XPS spectra (Figure 3c) were deconvoluted into four main peaks, present at the binding energy of 284.71, 285.70, 286.96, and 288.49 eV, which can be attributed to sp2 (C−C/C=C) domains of graphitic structures, C−O, C−N, and C=O functional groups, respectively.[39−41] It can be assumed that the N-doping of GQDs through the interaction with DETA molecules results in the appearance of C−N bonds by converting carbonyl (C=O) and epoxy (C−O) groups into amine/amide functionalities. Similarly, in the deconvoluted N 1s spectra (Figure 3d), four main peaks present at the binding energy of 399.4, 399.1, 398.3, and 397.5 eV can be assigned to amide-carbonyl (−NH−C=O), pyrrolic (C2−N−H), pyridinic (C−N−C), and amine (−NH2) functional groups, respectively.[28,39,40,42] Besides, quantitative XPS results show the presence of 59.54% carbon and 18.65% nitrogen, signifying that the prepared amine-N-GQDs are carbon-rich and sufficiently nitrogen-doped.

3.2. Molecular Simulations. For amine-N-GQDs structure optimization and in-depth analysis of FTIR and XPS spectra, to explore the presence of possible nitrogen doping (N-doping) and amine functionalization sites, molecular simulations were performed using Material Studio software of Dassault Systems (previously Accelrys Inc.).[43] The geometrical structure of amine-N-GQDs crystals was optimized using the BFGS algorithm after aptly selecting convergence
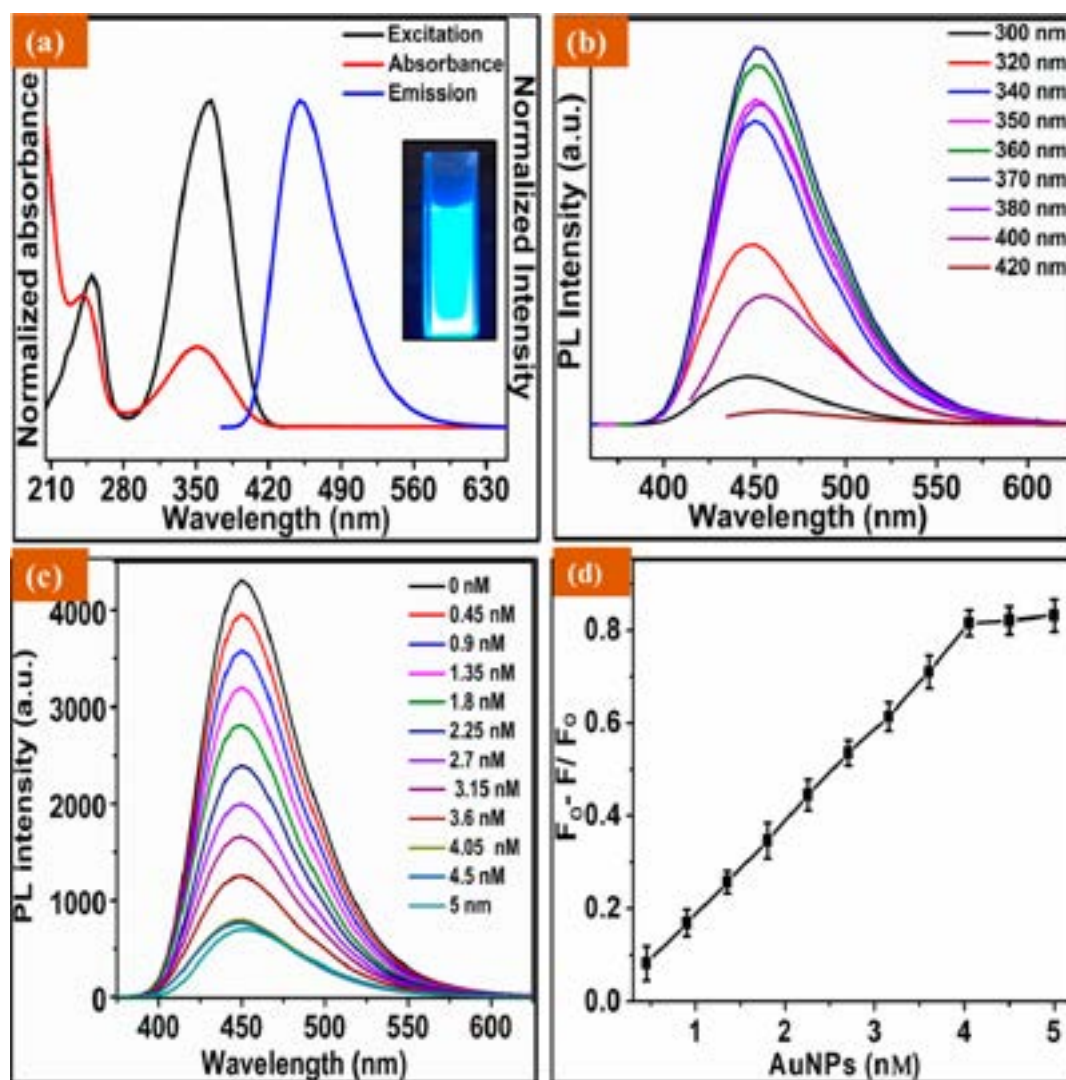
Figure 4. (a) Excitation (black line), emission (blue line), and absorbance (red line) spectra of amine-N-GQDs (inset: intense and bright blue colored fluorescence of amine-N-GQDs under the irradiation of 365 nm UV light); (b) PL spectra of amine-N-GQDs at different excitation wavelengths; (c) fluorescence spectra of anti-NSE/amine-N-GQDs nanoprobe with increasing quencher (AuNPs) concentration (0−5 nM from top to bottom); (d) quenching efficiency (QE) induced by different concentration of AuNPs.

tolerance parameters (maximum force, 0.05 eV/Å; energy, 2.0 × 10^{-5} eV/atom; maximum stress, 0.1 GPa; maximum displacement, 0.002 Å; maximum iterations, 100). The successfully optimized and relaxed atomic structure of amine-N-GQDs (Figure 3e) was compared with experimentally characterized structures for the validation of size, N-doping sites, and surface functionalization. It can be observed from Figure 3e that the size of the computationally optimized structure (∼3 nm) is in good accordance with the TEM results of as-synthesized amine-N-GQDs. Also, the various N-doping sites (pyrrolic (C2−N−H), pyridinic (C−N−C) N), amine, and amide functionalities observed from the theoretical structure are in decent agreement with XPS results.

Next, the FTIR spectrum of the theoretically optimized amine-N-GQDs structure (Figure 3f) was computationally calculated using vibrational analysis tools in Material Studio software. The peaks obtained at 2854 and 3252 cm^{-1} correspond to the stretching vibration of C−H and N−H amine/amide bonds, respectively. The appearance of a characteristic peak at 1621 cm^{-1} can be attributed to the bending vibration of N−H, and −NH−C=O. The additional peaks observed at 1554, 1372, 1242, and 1102 cm^{-1} can be ascribed to stretching vibrations of C=C present in GQDs framework, N−C=O, C−N in-plane stretching, and C−O, respectively. Interestingly, all the peaks observed in theoretically calculated FTIR spectrum for their respective bonds existing in the optimized structure are in good agreement with experimental FTIR results. From both experimental and theoretical results, it can be stated that DETA treatment during the hydrothermal synthesis results in the substitutional N-doping at the edge sites of GQDs. Moreover, the presence of amine and amide functionalities verified the successful surface functionalization.

3.3. Optical Characterizations. The absorption spectra of amine-N-GQDs (Figure 4a) exhibit an absorbance band around 240 nm, which might be ascribed to π−π* transition of C=C aromatic sp^2 atoms and the construction of multiple polyaromatic chromophores.[41] It has been reported that in the case of bare GQDs, the absorption peak obtained between 320 and 350 nm is generally assigned to n−π* transitions of C=O bonds, which disappears immediately after the reduction.[28] To verify this, we also performed the reduction of amine-N-GQDs

with NaBH$_4$ and further measured the absorbance and PL spectra. However, no significant change was observed in both spectra after the reduction reaction (Figure S4), signifying that the band present around 350 nm is not only because of n−π* transitions of C=O but also related to the C−N/C=N transitions due to N-doping of GQDs.[28] The absolute QY of synthesized amine-N-GQDs was obtained as high as 76.83% compared to pristine GQDs (14.57%), which is favorable for working as the energy donor. The high QY can be assigned to the combined effect of N-doping and amine functionalization of GQDs. N-doping introduces additional surface energy state and more active sites, which promotes radiative recombination resulting in improved fluorescence.[27] Furthermore, the surface functionalization converts the −COOH and epoxy groups of GQDs to −CNHR and −CONHR. These groups result in suppression of nonradiative electron−hole recombination and thereby enrich intrinsic state emission.[19] The PL spectra of amine-N-GQDs exhibited a broad emission band centered around 450 nm at the excitation wavelengths of 360 nm (Figure 4a). The picture in the inset of Figure 4a revealed the intense and bright blue colored fluorescence of amine-N-GQDs aqueous solution under the exposure of 365 nm UV light. Further, the results of the photoluminescence (PL) spectra of amine-N-GQDs (Figure 4b) under different excitation wavelengths (300−420 nm) demonstrated that the emission spectra are nearly excitation independent. The PL intensity was found to increase in the range of 300 to 370 nm and then gradually decreases.

3.4. Energy Transfer between Anti-NSE/Amine-N-GQDs and AuNPs. The selection of appropriate donor−acceptor pair has been found to be very important for highly efficient energy transfer. Moreover, it has been reported that there should be a substantial spectral overlap between the absorption spectrum of the acceptor and the emission spectrum of the donor.[44,45] Figure S5 indicated that the absorption spectra of AuNPs significantly overlap with the emission spectra of anti-NSE/amine-N-GQDs, ensuring that highly efficient energy transfer occurs between the selected donor−acceptor pair. Next, the anti-NSE/amine-N-GQDs conjugate was incubated with a series of AuNPs concentration (0-5 nM). Then the PL spectra of anti-NSE/amine-N-GQDs@AuNPs nanocomplex were recorded for this series of quencher concentrations. It has been observed that the PL intensity of anti-NSE/amine-N-GQDs conjugate gradually decreases as AuNPs concentration increases without any shift in peak position (Figure 4c). This quenching has been induced by the dipole-surface interactions between anti-NSE/amine-N-GQDs conjugate and AuNPs, which brings them in close proximity to transfer the excited state energy to AuNPs.[17] This self-assembled anti-NSE/amine-N-GQDs@AuNPs nanocomplex acts as a fluorescent nanoprobe for the target biomarker detection. The quenching efficiency (QE) has been calculated using eq 1:

$$QE = F_0 - F/F_0 \tag{1}$$

where F_0 is the PL intensity of anti-NSE/amine-N-GQDs conjugate solution incubated with only PBS (no quencher), and F is the PL intensity of anti-NSE/amine-N-GQDs conjugate in the presence of quencher. The maximum quenching efficiency (Figure 4d) was calculated to be 81.5% with 4.05 nM AuNPs concentration. After that, the PL intensity was found almost unchanged, signifying the completion of the quenching between anti-NSE/amine-N-

GQDs and AuNPs. Thus, 4.05 nM was selected as the optimal concentration and used for further experiments. Further, to analyze the quenching mechanism, the Stern−Volmer plot, that is, the relative change in fluorescence intensity (F_0/F) as a function of quencher concentration [AuNPs] has been studied (Figure S6). This plot has been found to be nonlinear with upward curvature signifying that both static and dynamic quenching processes are involved in the sensing system. Next, time-resolved PL spectroscopy was performed to investigate the dynamics of energy transfer for the selected donor−acceptor pair (Figure S7). It was observed that the fluorescence lifetime of anti-NSE/amine-N-GQDs conjugate decreases significantly after the addition of AuNPs, specifying the energy transfer process from the biofunctionalized conjugate to AuNPs.[17,46] The energy transfer efficiency between the selected pair was calculated using eq 2:

$$\phi_E = 1 - \frac{\tau_{DA}}{\tau_D} \tag{2}$$

where τ_D is the decay lifetime of anti-NSE/amine-N-GQDs conjugate without acceptor (AuNPs), and τ_{DA} is the lifetime of anti-NSE/amine-N-GQDs conjugate with energy acceptor. The energy transfer efficiency between the selected pair was obtained to be 42.9%. This nonradiative energy transfer between donor−acceptor pair can be modeled as dipole to surface energy transfer and has been explained by following the NSET mechanism as described previously.[17,18] The critical distance R_0, where energy transfer efficiency is 50%, was calculated using the Persson-Lang model (eq 3):

$$R_0 = \left[\frac{0.225c^3\Phi_D}{\omega_D{}^2\omega_F k_f} \right]^{1/4} \tag{3}$$

where Φ_D is the donor quantum yield (0.76) without acceptor, c is the speed of light, ω_D is the donor angular frequency (4.2 × 10^{15} s^{-1}), and k_f (1.2 × 10^{10} cm^{-1}) and ω_F (8.4 × 10^{15} s^{-1}) are the Fermi vector and angular frequency of bulk gold, respectively. The critical distance R_0 for the selected pair was obtained to be 7.1 nm. Subsequently, the distance between the chosen donor−acceptor pair (r) was calculated using eq 4:

$$r = R_0 \left[\frac{\tau_{DA}}{\tau_D - \tau_{DA}} \right]^{1/4} \tag{4}$$

where τ_D is the decay lifetime of anti-NSE/amine-N-GQDs conjugate without acceptor (AuNPs), and τ_{DA} is the lifetime of anti-NSE/amine-N-GQDs conjugate with the acceptor. The distance (r) was obtained to be 8.8 nm. The calculated distance was obtained well within the limit of forming NSET pair for energy transfer.[17,47]

3.5. Detection of NSE Biomarker. First, to realize the NSE biomarker detection, the effect of pH on the PL intensity of anti-NSE/amine-N-GQDs conjugate has been investigated (details in Supporting Information, Figure S8). Then different concentrations of the NSE antigen (0.1 pg mL^{-1} to 1000 ng mL^{-1}) were prepared by diluting the obtained stock solution. After that, the anti-NSE/amine-N-GQDs@AuNPs nanocomplex solution was optimized for the minimum response time required to recover the quenched fluorescence intensity. Fifty microliters of NSE antigen (1 ng mL^{-1}) was added into the anti-NSE/amine-N-GQDs@AuNPs nanocomplex solution. After the NSE antigen was added, the nanocomplex solution was allowed to incubate for the different time duration (2 to 32
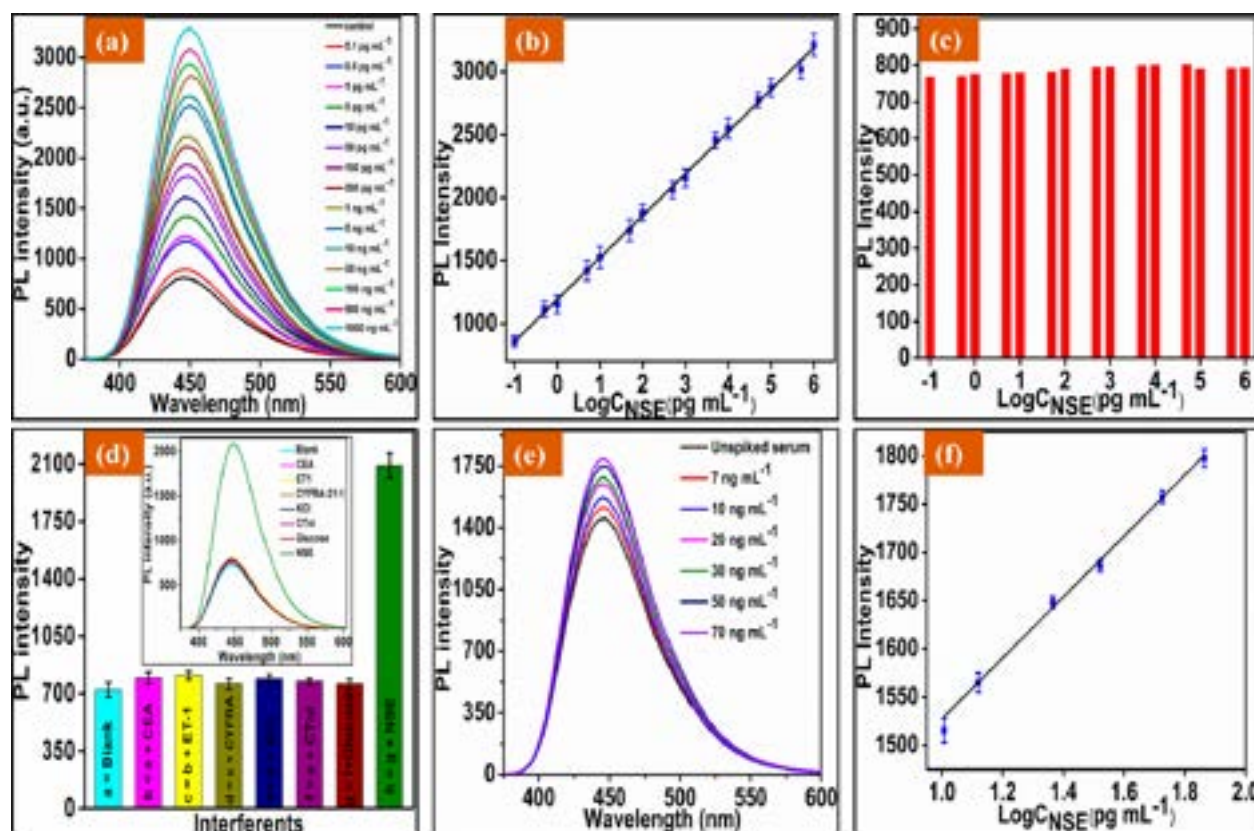
Figure 5. (a) Fluorescence response studies of anti-NSE/amine-N-GQDs@AuNPs nanoprobe as a function of NSE antigen concentration (0.1 pg mL^{-1} to 1000 ng mL^{-1} from bottom to top); (b) calibration curve indicating the linear relationship between log concentration of NSE and PL intensity of the nanoprobe; (c) control experiment of amine-N-GQDs@AuNPs as a function of log concentration of NSE antigen and PL intensity; (d) selectivity studies of anti-NSE/amine-N-GQDs@AuNPs nanoprobe with different interferents (inset shows their corresponding PL spectra); (e) PL curves indicating the fluorescence response of anti-NSE/amine-N-GQDs@AuNPs nanoprobe toward spiked serum samples (7, 10, 20, 30, 50, and 70 ng mL^{-1}); (f) calibration curve for the spiked serum samples indicating the linear relationship between log concentration of NSE and PL intensity of the nanoprobe.

min) to have efficient immunoreaction and obstruction in the energy transfer process to recover the fluorescence. Figure S9 indicates that the PL intensity recovered gradually, reaching the highest value at 16 min, after which no significant increase was obtained in the PL intensity. Therefore, the optimum response time has been selected to be 16 min for the NSE detection, during which the immunoreaction attains the steady-state condition. Figure 5a shows the PL response of the anti-NSE/amine-N-GQDs@AuNPs nanocomplex for the different NSE antigen concentrations (0.1 pg mL^{-1} to 1000 ng mL^{-1}). Fluorescence intensity of anti-NSE/amine-N-GQDs conjugate was found to recover linearly with increasing NSE antigen concentration (Figure 5b) and can be described by the eq 5:

$$I = 333.20 \log_{10} \text{NSE (pg mL}^{-1}\text{)} + 1190.84$$

$$\text{Regression coefficient } R^2 = 0.998 \tag{5}$$

The PL intensity recovery can be attributed to the formation of immunocomplex arising due to the specific interaction of NSE antigen with anti-NSE antibody, which increases the distance between anti-NSE/amine-N-GQDs donor and AuNPs quencher resulting in the obstruction of the energy transfer process and hence gradual recovery of fluorescence.[48,49] Further, the limit of detection (LOD) was found to be 0.09 pg mL^{-1} calculated using the eq 6:

$$\text{LOD} = \frac{3\sigma}{S} \tag{6}$$

where σ is the standard deviation, and S is the sensitivity of the fluorescent biosensor calculated using the slope of the calibration curve.

3.6. Control Experiment, Selectivity, and Reproducibility Studies. A control experiment was conducted to investigate the PL response of amine-N-GQDs@AuNPs nanocomplex as a function of NSE antigen (0.1 pg mL^{-1} to 1000 ng mL^{-1}). No significant recovery in the fluorescence of amine-N-GQDs was obtained with increasing NSE antigen concentration (Figure 5c), signifying that the NSE antigen does not interact with the amine-N-GQDs@AuNPs to form the antigen−antibody immunocomplex. Therefore, there will be no obstruction in the energy transfer process to recover the fluorescence. Next, the selectivity study of the fluorescent biosensor (Figure 5d) was performed by incubating the amine-N-GQDs@AuNPs nanocomplex with different interfering substances such as carcinoembryonic antigen (CEA), endothelin-1 (ET-1), cardiac troponin-I (cTnI), potassium chloride (KCl), cytokeratin-19 fragment (CYFRA-21−1), and glucose known to be present in serum samples. The nanocomplex was incubated with 50 μL of each interferant one by one in the same solution, and their corresponding PL spectra were measured. A negligible change in the magnitude of fluorescence intensity was observed in the presence of these

Table 1. Characteristics of Different Biosensing Platforms and Detection Techniques Used for NSE Detection

sr. no.	biosensing platform used	detection technique	detection range (ng mL^{-1})	LOD	time (min)	ref
1.	anti-NSE/ZnCdHgSe QDs/PDPIT/ITO	Photoelectrochemical	0.001–100	0.2 pg mL^{-1}	30	50
2.	anti-NSE/CSnanoAu/APTES/PBSiO$_2$/GCE	Amperometric	0.25–75.0	0.08 ng mL^{-1}	35	51
3.	AP-anti-IgG/AuNPs/anti-NSE/NSESWNTs/GCE	Electrochemical	0.10–2000	0.03 ng mL^{-1}	60	52
4.	anti-NSE/Au–Gra/NiHCFNPs/AuNCs/GCE	Electrochemical	0.001–100	0.3 pg mL^{-1}	30	53
5.	PPD-GR/AuNPs/anti-NSE/SPE	Electrochemical	1–1000	0.3 ng mL^{-1}	60	3
6.	Anti-NSE/NSE/anti-NSE-biotin/streptavidin/FITC/QDs	Fluorescence	3–100	1.0 ng mL^{-1}		54
7.	CaCO$_3$/AuNCs hybrid	Fluorescence Electrochemical	0.005–1 0.0005–2	2.0 pg mL^{-1} 0.1 pg mL^{-1}	30	55
8.	FITC-anti-NSE/ALP-NSE/anti-FITC-MB	Chemiluminscence	0–300	0.2 ng mL^{-1}		56
9.	anti-NSE/DA/TiO$_2$/FTO	Photoelectrochemical	0.1–1000	0.05 ng mL^{-1}	30	57
10.	NH2-G/Thi/AuNPs POCT	Wireless POCT	1–500	10 pg mL^{-1}	18	58
11.	anti-NSE/amine-N-GQDs @AuNPs	NSET	0.0001–1000	0.09 pg mL^{-1}	16	This work

interferants compared to the blank (amine-N-GQDs@AuNPs). The variation (recovery) in the fluorescence intensity was found to be less than 5%. However, upon the addition of target NSE, antigen fluorescence intensity recovered significantly, validating the good selectivity of fabricated biosensor toward NSE detection. Also, the selectivity coefficient (SC) for each interferant was found to be ~1, calculated using eq 7:

$$SC = \frac{I_{C+I}}{I_C}$$

(7)

where I_{C+I} is the magnitude of PL intensity in the presence of the interferant, while I_C is the magnitude of PL intensity in the absence of the interferant. The reproducibility of the fluorescent biosensor was investigated by measuring the fluorescence recovery of six different nanoprobes (anti-NSE/amine-N-GQDs@AuNPs) fabricated under similar conditions and incubated with same NSE antigen concentration (1 ng mL^{-1}). Similar results with a calculated relative standard deviation (% RSD) of 1.85 from all of the nanoprobes signifies the high reproducibility of the fabricated biosensor (Figure S10).

3.7. Real Sample Analysis. In this context, first, the blood was collected in a sterilized tube from a healthy person after taking his written consent and approval from the institutional Ethical and Biosafety committee (BT/IHEC-IITR/2019/7525) and further centrifuged at 4000 rpm to obtain the clear serum. After that, to quantify the feasibility of the fluorescent biosensor in real samples, serum of a healthy human was spiked with six different NSE antigen concentrations (7, 10, 20, 30, 50, and 70 ng mL^{-1}), and the response was measured using PL (Figure 5e). Similar to the previous experiment, the nanocomplex solution (anti-NSE/amine-N-GQDs@AuNPs) was incubated for the optimized incubation time of 16 min after addition of NSE spiked serum samples to have efficient immunoreaction. A similar kind of trend, indicating increase (recovery) in the fluorescence intensity with increasing NSE concentration, has been obtained for the spiked serum samples. The calibration curve (Figure 5f) shows a linear relationship between PL intensity and six NSE antigen spiked serum samples and fit according to eq 8:

$$I = 315.83 \log_{10} NSE \ (pg \ mL^{-1}) + 1211.79$$

Regression coefficient $R^2 = 0.992$

(8)

The % recovery of NSE in the serum samples has been calculated utilizing eq 9 and has been indicated in Table S1:

$$\% \ recovery = \frac{y_I - y_o}{ys} \times 100$$

(9)

where y_o and y_I are the obtained concentrations of the NSE in unspiked and spiked samples from the calibration plot of standard samples, and y_s is the actual concentration of spiked NSE. The fluorescent biosensor revealed an average recovery of 94.69% for NSE antigen in spiked serum samples, signifying the high efficiency of the fluorescent biosensor for NSE detection in real samples. Finally, comparison of the proposed fluorescent biosensor with the previously reported biosensors for NSE detection has been shown in Table 1.

4. CONCLUSIONS

We have demonstrated the fabrication and application of fluorescent biosensor for the quantitative and ultrasensitive NSE detection utilizing biofunctionalized graphene quantum dots as an energy donor and AuNPs as the acceptor. The bottom-up hydrothermal method provided uniform and small-sized (~3 nm) amine-N-GQDs with excellent optical properties, namely high absolute QY ≈ 76.83%, excitation independent, blue colored, strong and stable fluorescence, longer fluorescence decay lifetime (13.1 ns). The structure of synthesized amine-N-GQDs has been successfully estimated through the molecular simulation studies. Both theoretical and experimental characterization tools verified the successful N-doping and amine functionalization. The MTT assay results provided the high cell viability (81.5% for A549 and 84.5% for L-132) even at higher concentration (1000 μg mL^{-1}). Efficient quenching efficiency of 81.5% and energy transfer efficiency of 42.9% have been obtained with the selected donor–acceptor pair. The developed NSE/anti-NSE/amine-N-GQDs@AuNPs fluorescent turn-on biosensor was successfully utilized for NSE biomarker detection with remarkable biosensing parameters including fast response time (16 min), wider linear detection range (0.1 pg mL^{-1} to 1000 ng mL^{-1}), excellent selectivity, and remarkable low detection limit (0.09 pg mL^{-1}). The

fluorescent biosensor also exhibited excellent performance in real samples, with an average recovery of 94.69%. This amine-N-GQDs based fluorescent biosensor development opens a new window for the widespread utilization of evolving zero-dimensional fluorescent materials in various biomedical applications including biosensing, bioimaging, gene delivery, drug delivery, and 3D printed implantable biochip.

■ ASSOCIATED CONTENT

Ⓢ Supporting Information

The Supporting Information is available free of charge at https://pubs.acs.org/doi/10.1021/acsabm.0c00427.

Chemicals and reagents, instrumentation, synthesis of gold nanoparticles (AuNPs), characterizations of bio-functionalized conjugate, calculation of adhesion efficiency, cytotoxicity studies, PL emission and UV−vis spectra of amine-N-GQDs before and after reduction, overlap between absorption and emission spectra, Stern−Volmer plot, time resolved PL spectroscopy studies, pH study, response time and reproducibility study graphs, estimation of NSE in spiked serum samples (PDF)

■ AUTHOR INFORMATION

Corresponding Author

Gopinath Packirisamy − *Department of Biotechnology and Centre for Nanotechnology, Indian Institute of Technology Roorkee, Roorkee, Uttarakhand 247667, India;* ⓘ orcid.org/0000-0003-1379-1203; Phone: +91-1332-285650; Email: gopi@bt.iitr.ac.in, genegopi@gmail.com; Fax: +91-1332-273560

Authors

Ashish Kalkal − *Department of Biotechnology, Indian Institute of Technology Roorkee, Roorkee, Uttarakhand 247667, India;* ⓘ orcid.org/0000-0002-4342-1193

Rangadhar Pradhan − *Centre for Nanotechnology, Indian Institute of Technology Roorkee, Roorkee, Uttarakhand 247667, India;* ⓘ orcid.org/0000-0002-9283-4955

Sachin Kadian − *Department of Polymer and Process Engineering, Indian Institute of Technology Roorkee, Roorkee, Uttrakhand 247667, India;* ⓘ orcid.org/0000-0002-2804-1109

Gaurav Manik − *Department of Polymer and Process Engineering, Indian Institute of Technology Roorkee, Roorkee, Uttrakhand 247667, India;* ⓘ orcid.org/0000-0003-2501-1737

Complete contact information is available at:
https://pubs.acs.org/10.1021/acsabm.0c00427

Author Contributions

[⊥]These authors contributed equally to work.

Notes

The authors declare no competing financial interest.

■ REFERENCES

(1) Stovold, R.; Blackhall, F.; Meredith, S.; Hou, J.; Dive, C.; White, A. Biomarkers for small cell lung cancer: Neuroendocrine, epithelial and circulating tumour cells. *Lung Cancer* **2012**, *76* (3), 263−268.

(2) Arya, S. K.; Bhansali, S. Lung Cancer and Its Early Detection Using Biomarker-Based Biosensors. *Chem. Rev.* **2011**, *111* (11), 6783−6809.

(3) Amani, J.; Maleki, M.; Khoshroo, A.; Sobhani-Nasab, A.; Rahimi-Nasrabadi, M. An electrochemical immunosensor based on poly p-phenylenediamine and graphene nanocomposite for detection of neuron-specific enolase via electrochemically amplified detection. *Anal. Biochem.* **2018**, *548*, 53−59.

(4) Shi, J.; Tian, F.; Lyu, J.; Yang, M. Nanoparticle based fluorescence resonance energy transfer (FRET) for biosensing applications. *J. Mater. Chem. B* **2015**, *3* (35), 6989−7005.

(5) Youssef, S.; Zhang, S.; Ai, H.-w. A Genetically Encoded, Ratiometric Fluorescent Biosensor for Hydrogen Sulfide. *ACS Sensors* **2019**, *4* (6), 1626−1632.

(6) Lau, D.; Walsh, J. C.; Peng, W.; Shah, V. B.; Turville, S.; Jacques, D. A.; Böcking, T. Fluorescence Biosensor for Real-Time Interaction Dynamics of Host Proteins with HIV-1 Capsid Tubes. *ACS Appl. Mater. Interfaces* **2019**, *11* (38), 34586−34594.

(7) Della Ventura, B.; Gelzo, M.; Battista, E.; Alabastri, A.; Schirato, A.; Castaldo, G.; Corso, G.; Gentile, F.; Velotta, R. Biosensor for Point-of-Care Analysis of Immunoglobulins in Urine by Metal Enhanced Fluorescence from Gold Nanoparticles. *ACS Appl. Mater. Interfaces* **2019**, *11* (4), 3753−3762.

(8) Fu, Y.; Chen, T.; Wang, G.; Gu, T.; Xie, C.; Huang, J.; Li, X.; Best, S.; Han, G. Production of a fluorescence resonance energy transfer (FRET) biosensor membrane for microRNA detection. *J. Mater. Chem. B* **2017**, *5* (34), 7133−7139.

(9) Wang, G.; He, P.; Xu, A.; Guo, Q.; Li, J.; Wang, Z.; Liu, Z.; Chen, D.; Yang, S.; Ding, G. Promising Fast Energy Transfer System Between Graphene Quantum Dots and the Application in Fluorescent Bioimaging. *Langmuir* **2019**, *35* (3), 760−766.

(10) Das, P.; Sedighi, A.; Krull, U. J. Cancer biomarker determination by resonance energy transfer using functional fluorescent nanoprobes. *Anal. Chim. Acta* **2018**, *1041*, 1−24.

(11) Ma, F.; Li, C.-c.; Zhang, C.-y. Development of quantum dot-based biosensors: principles and applications. *J. Mater. Chem. B* **2018**, *6* (39), 6173−6190.

(12) Wolfbeis, O. S. Materials for fluorescence-based optical chemical sensors. *J. Mater. Chem.* **2005**, *15* (27−28), 2657−2669.

(13) Yang, S.; Sun, J.; Li, X.; Zhou, W.; Wang, Z.; He, P.; Ding, G.; Xie, X.; Kang, Z.; Jiang, M. Large-scale fabrication of heavy doped carbon quantum dots with tunable-photoluminescence and sensitive fluorescence detection. *J. Mater. Chem. A* **2014**, *2* (23), 8660−8667.

(14) Biju, V.; Itoh, T.; Ishikawa, M. Delivering quantum dots to cells: bioconjugated quantum dots for targeted and nonspecific extracellular and intracellular imaging. *Chem. Soc. Rev.* **2010**, *39* (8), 3031−3056.

(15) Sun, J.; Yang, S.; Wang, Z.; Shen, H.; Xu, T.; Sun, L.; Li, H.; Chen, W.; Jiang, X.; Ding, G.; Kang, Z.; Xie, X.; Jiang, M. Ultra-High Quantum Yield of Graphene Quantum Dots: Aromatic-Nitrogen Doping and Photoluminescence Mechanism. *Particle & Particle Systems Characterization* **2015**, *32* (4), 434−440.

(16) Yang, S.; Sun, J.; He, P.; Deng, X.; Wang, Z.; Hu, C.; Ding, G.; Xie, X. Selenium Doped Graphene Quantum Dots as an Ultrasensitive Redox Fluorescent Switch. *Chem. Mater.* **2015**, *27* (6), 2004−2011.

(17) Chen, C.; Midelet, C.; Bhuckory, S.; Hildebrandt, N.; Werts, M. H. V. Nanosurface Energy Transfer from Long-Lifetime Terbium

Donors to Gold Nanoparticles. *J. Phys. Chem. C* **2018**, *122* (30), 17566−17574.

(18) Chen, C.; Hildebrandt, N. Resonance energy transfer to gold nanoparticles: NSET defeats FRET. *TrAC, Trends Anal. Chem.* **2020**, *123*, 115748.

(19) Zhu, S.; Zhang, J.; Tang, S.; Qiao, C.; Wang, L.; Wang, H.; Liu, X.; Li, B.; Li, Y.; Yu, W.; Wang, X.; Sun, H.; Yang, B. Surface Chemistry Routes to Modulate the Photoluminescence of Graphene Quantum Dots: From Fluorescence Mechanism to Up-Conversion Bioimaging Applications. *Adv. Funct. Mater.* **2012**, *22* (22), 4732−4740.

(20) Zheng, X. T.; Ananthanarayanan, A.; Luo, K. Q.; Chen, P. Glowing Graphene Quantum Dots and Carbon Dots: Properties, Syntheses, and Biological Applications. *Small* **2015**, *11* (14), 1620−1636.

(21) Li, R. S.; Yuan, B.; Liu, J. H.; Liu, M. L.; Gao, P. F.; Li, Y. F.; Li, M.; Huang, C. Z. Boron and nitrogen co-doped single-layered graphene quantum dots: a high-affinity platform for visualizing the dynamic invasion of HIV DNA into living cells through fluorescence resonance energy transfer. *J. Mater. Chem. B* **2017**, *5* (44), 8719−8724.

(22) Kadian, S.; Manik, G.; Das, N.; Nehra, P.; Chauhan, R. P.; Roy, P. Synthesis, characterization and investigation of synergistic antibacterial activity and cell viability of silver−sulfur doped graphene quantum dot (Ag@S-GQDs) nanocomposites. *J. Mater. Chem. B* **2020**, *8* (15), 3028−3037.

(23) Zhu, C.; Yang, S.; Wang, G.; Mo, R.; He, P.; Sun, J.; Di, Z.; Yuan, N.; Ding, J.; Ding, G.; Xie, X. Negative induction effect of graphite N on graphene quantum dots: tunable band gap photo-luminescence. *J. Mater. Chem. C* **2015**, *3* (34), 8810−8816.

(24) Huang, H.; Yang, S.; Liu, Y.; Yang, Y.; Li, H.; McLeod, J. A.; Ding, G.; Huang, J.; Kang, Z. Photocatalytic Polymerization from Amino Acid to Protein by Carbon Dots at Room Temperature. *ACS Applied Bio Materials* **2019**, *2* (11), 5144−5153.

(25) Kadian, S.; Manik, G.; Kalkal, A.; Singh, M.; Chauhan, R. P. Effect of sulfur doping on fluorescence and quantum yield of graphene quantum dots: an experimental and theoretical investigation. *Nanotechnology* **2019**, *30* (43), 435704.

(26) Zhu, J.; Tang, Y.; Wang, G.; Mao, J.; Liu, Z.; Sun, T.; Wang, M.; Chen, D.; Yang, Y.; Li, J.; Deng, Y.; Yang, S. Green, Rapid, and Universal Preparation Approach of Graphene Quantum Dots under Ultraviolet Irradiation. *ACS Appl. Mater. Interfaces* **2017**, *9* (16), 14470−14477.

(27) Qu, D.; Zheng, M.; Zhang, L.; Zhao, H.; Xie, Z.; Jing, X.; Haddad, R. E.; Fan, H.; Sun, Z. Formation mechanism and optimization of highly luminescent N-doped graphene quantum dots. *Sci. Rep.* **2015**, *4*, 5294.

(28) Qu, D.; Zheng, M.; Li, J.; Xie, Z.; Sun, Z. Tailoring color emissions from N-doped graphene quantum dots for bioimaging applications. *Light: Sci. Appl.* **2015**, *4*, e364.

(29) Liu, S.; Tian, J.; Wang, L.; Zhang, Y.; Qin, X.; Luo, Y.; Asiri, A. M.; Al-Youbi, A. O.; Sun, X. Hydrothermal Treatment of Grass: A Low-Cost, Green Route to Nitrogen-Doped, Carbon-Rich, Photo-luminescent Polymer Nanodots as an Effective Fluorescent Sensing Platform for Label-Free Detection of Cu(II) Ions. *Adv. Mater.* **2012**, *24* (15), 2037−2041.

(30) Yang, S.; Sun, J.; Zhu, C.; He, P.; Peng, Z.; Ding, G. Supramolecular recognition control of polyethylene glycol modified N-doped graphene quantum dots: tunable selectivity for alkali and alkaline-earth metal ions. *Analyst* **2016**, *141* (3), 1052−1059.

(31) Li, J.; Yang, S.; Deng, Y.; Chai, P.; Yang, Y.; He, X.; Xie, X.; Kang, Z.; Ding, G.; Zhou, H.; Fan, X. Emancipating Target-Functionalized Carbon Dots from Autophagy Vesicles for a Novel Visualized Tumor Therapy. *Adv. Funct. Mater.* **2018**, *28* (30), 1800881.

(32) Vashist, S. K.; Lam, E.; Hrapovic, S.; Male, K. B.; Luong, J. H. T. Immobilization of Antibodies and Enzymes on 3-Aminopropyl-triethoxysilane-Functionalized Bioanalytical Platforms for Biosensors and Diagnostics. *Chem. Rev.* **2014**, *114* (21), 11083−11130.

(33) Biju, V. Chemical modifications and bioconjugate reactions of nanomaterials for sensing, imaging, drug delivery and therapy. *Chem. Soc. Rev.* **2014**, *43* (3), 744−764.

(34) Xu, S.; Dong, B.; Zhou, D.; Yin, Z.; Cui, S.; Xu, W.; Chen, B.; Song, H. Paper-based upconversion fluorescence resonance energy transfer biosensor for sensitive detection of multiple cancer biomarkers. *Sci. Rep.* **2016**, *6*, 23406.

(35) Kumar, S.; Ashish; Kumar, S.; Augustine, S.; Yadav, S.; Yadav, B. K.; Chauhan, R. P.; Dewan, A. K.; Malhotra, B. D. Effect of Brownian motion on reduced agglomeration of nanostructured metal oxide towards development of efficient cancer biosensor. *Biosens. Bioelectron.* **2018**, *102*, 247−255.

(36) Mayilo, S.; Kloster, M. A.; Wunderlich, M.; Lutich, A.; Klar, T. A.; Nichtl, A.; Kürzinger, K.; Stefani, F. D.; Feldmann, J. Long-Range Fluorescence Quenching by Gold Nanoparticles in a Sandwich Immunoassay for Cardiac Troponin T. *Nano Lett.* **2009**, *9* (12), 4558−4563.

(37) Sidhu, J. S.; Singh, A.; Garg, N.; Kaur, N.; Singh, N. Gold conjugated carbon dots nano assembly: FRET paired fluorescence probe for cysteine recognition. *Sens. Actuators, B* **2019**, *282*, 515−522.

(38) Wu, Z. L.; Gao, M. X.; Wang, T. T.; Wan, X. Y.; Zheng, L. L.; Huang, C. Z. A general quantitative pH sensor developed with Dicyandiamide N-doped high quantum yield graphene quantum dots. *Nanoscale* **2014**, *6* (7), 3868−3874.

(39) Kuo, W.-S.; Shao, Y.-T.; Huang, K.-S.; Chou, T.-M.; Yang, C.-H. Antimicrobial Amino-Functionalized Nitrogen-Doped Graphene Quantum Dots for Eliminating Multidrug-Resistant Species in Dual-Modality Photodynamic Therapy and Bioimaging under Two-Photon Excitation. *ACS Appl. Mater. Interfaces* **2018**, *10* (17), 14438−14446.

(40) Sandeep Kumar, G.; Roy, R.; Sen, D.; Ghorai, U. K.; Thapa, R.; Mazumder, N.; Saha, S.; Chattopadhyay, K. K. Amino-functionalized graphene quantum dots: origin of tunable heterogeneous photo-luminescence. *Nanoscale* **2014**, *6* (6), 3384−3391.

(41) Zheng, M.; Xie, Z.; Qu, D.; Li, D.; Du, P.; Jing, X.; Sun, Z. On−Off−On Fluorescent Carbon Dot Nanosensor for Recognition of Chromium(VI) and Ascorbic Acid Based on the Inner Filter Effect. *ACS Appl. Mater. Interfaces* **2013**, *5* (24), 13242−13247.

(42) Zhai, X.; Zhang, P.; Liu, C.; Bai, T.; Li, W.; Dai, L.; Liu, W. Highly luminescent carbon nanodots by microwave-assisted pyrolysis. *Chem. Commun.* **2012**, *48* (64), 7955−7957.

(43) *Material Studio*; Dassault Systemes BIOVIA: UK, 2020.

(44) Nair, R. R.; Debnath, S.; Das, S.; Wakchaure, P.; Ganguly, B.; Chatterjee, P. B. A Highly Selective Turn-On Biosensor for Measuring Spermine/Spermidine in Human Urine and Blood. *ACS Applied Bio Materials* **2019**, *2* (6), 2374−2387.

(45) Sukumar, U. K.; Packirisamy, G. Fabrication of Nanofibrous Scaffold Grafted with Gelatin Functionalized Polystyrene Micro-spheres for Manifesting Nanomechanical Cues of Stretch Stimulated Fibroblast. *ACS Applied Bio Materials* **2019**, *2* (12), 5323−5339.

(46) Ghosh, D.; Chattopadhyay, N. J. O. Gold nanoparticles: acceptors for efficient energy transfer from the photoexcited fluorophores. *Opt. Photonics J.* **2013**, *3* (1), 18−26.

(47) Ashish; Ahmad, N.; Gopinath, P.; Vinogradov, A.; Ahmad, N.; Gopinath, P.; Dutta, R. Chapter 1 - 3D Printing in Medicine: Current Challenges and Potential Applications. *3D Printing Technology in Nanomedicine* **2019**, 1−22.

(48) Augustine, S.; Kumar, P.; Malhotra, B. D. Amine-Function-alized MoO3@RGO Nanohybrid-Based Biosensor for Breast Cancer Detection. *ACS Applied Bio Materials* **2019**, *2* (12), 5366−5378.

(49) Dorsey, M. P.; Nguelifack, B. M.; Yates, E. A. Colorimetric Detection of Mutant *β*-Amyloid(1−40) Membrane-Active Aggrega-tion with Biosensing Vesicles. *ACS Applied Bio Materials* **2019**, *2* (11), 4966−4977.

(50) Yu, X.; Wang, Y.; Chen, X.; Wu, K.; Chen, D.; Ma, M.; Huang, Z.; Wu, W.; Li, C. White-Light-Exciting, Layer-by-Layer-Assembled ZnCdHgSe Quantum Dots/Polymerized Ionic Liquid Hybrid Film for Highly Sensitive Photoelectrochemical Immunosensing of Neuron Specific Enolase. *Anal. Chem.* **2015**, *87* (8), 4237−4244.

(51) Zhong, Z.; Shan, J.; Zhang, Z.; Qing, Y.; Wang, D. The Signal-Enhanced Label-Free Immunosensor Based on Assembly of Prussian Blue-SiO2 Nanocomposite for Amperometric Measurement of Neuron-Specific Enolase. *Electroanalysis* **2010**, *22* (21), 2569−2575.

(52) Yu, T.; Cheng, W.; Li, Q.; Luo, C.; Yan, L.; Zhang, D.; Yin, Y.; Ding, S.; Ju, H. Electrochemical immunosensor for competitive detection of neuron specific enolase using functional carbon nanotubes and gold nanoprobe. *Talanta* **2012**, *93*, 433−438.

(53) Han, J.; Zhuo, Y.; Chai, Y.-Q.; Yuan, Y.-L.; Yuan, R. Novel electrochemical catalysis as signal amplified strategy for label-free detection of neuron-specific enolase. *Biosens. Bioelectron.* **2012**, *31* (1), 399−405.

(54) Li, H.; Cao, Z.; Zhang, Y.; Lau, C.; Lu, J. Simultaneous detection of two lung cancer biomarkers using dual-color fluorescence quantum dots. *Analyst* **2011**, *136* (7), 1399−1405.

(55) Peng, J.; Feng, L.-N.; Zhang, K.; Li, X.-H.; Jiang, L.-P.; Zhu, J.-J. Calcium Carbonate−Gold Nanocluster Hybrid Spheres: Synthesis and Versatile Application in Immunoassays. *Chem. - Eur. J.* **2012**, *18* (17), 5261−5268.

(56) Fu, X.; Meng, M.; Zhang, Y.; Yin, Y.; Zhang, X.; Xi, R. Chemiluminescence enzyme immunoassay using magnetic nano-particles for detection of neuron specific enolase in human serum. *Anal. Chim. Acta* **2012**, *722*, 114−118.

(57) Li, H.; Xiao, Q.; Lv, J.; Lei, Q.; Huang, Y. Dopamine modified hyperbranched TiO2 arrays based ultrasensitive photoelectrochemical immunosensor for detecting neuron specific enolase. *Anal. Biochem.* **2017**, *531*, 48−55.

(58) Fan, Y.; Liu, J.; Wang, Y.; Luo, J.; Xu, H.; Xu, S.; Cai, X. A wireless point-of-care testing system for the detection of neuron-specific enolase with microfluidic paper-based analytical devices. *Biosens. Bioelectron.* **2017**, *95*, 60−66.